

New abundance determinations in $z < 1.5$ QSO absorbers: seven sub-DLAs and one DLA.

Joseph D. Meiring¹, James T. Lauroesch^{2,3}, Varsha P. Kulkarni¹, Celine Péroux⁴, Pushpa Khare⁵, Donald G. York^{6,7}, & Arlin P. S. Crotts⁸

¹*Department of Physics and Astronomy, University of South Carolina, Columbia, SC 29208, USA*

²*Department of Physics and Astronomy, Northwestern University, Evanston, IL 60208, USA*

³*Department of Physics and Astronomy, University of Louisville, Louisville, Ky 40292 USA*

⁴*European Southern Observatory, Garching-bei-Munchen, Germany*

⁵*Department of Physics, Utkal University, Bhubaneswar, 751004, India*

⁶*Department of Astronomy and Astrophysics, University of Chicago, Chicago, IL 60637, USA*

⁷*Enrico Fermi Institute, University of Chicago, Chicago, IL 60637, USA*

⁸*Department of Astronomy, Columbia University, New York, NY 10027, USA*

Accepted ... Received ...; in original form ...

ABSTRACT

We present chemical abundance measurements from high resolution observations of 7 sub-damped Lyman- α absorbers and 1 damped Lyman- α system at $z < 1.5$. Three of these objects have high metallicity, with near or super-solar Zn abundance. Grids of Cloudy models for each system were constructed to look for possible ionization effects in these systems. For the systems in which we could constrain the ionization parameter, we find that the ionization corrections as predicted by the Cloudy models are generally small and within the typical error bars (~ 0.15 dex), in general agreement with previous studies. The Al III to Al II ratio for these and other absorbers from the literature are compared, and we find that while the sub-DLAs have a larger scatter in the Al III to Al II ratios than the DLAs, there appears to be little correlation between the ratio and $N_{\text{H I}}$. The relationship between the metallicity and the velocity width of the profile for these systems is investigated. We show that the sub-DLAs that have been observed to date follow a similar trend as DLA absorbers, with the more metal rich systems exhibiting large velocity widths. We also find that the systems at the upper edge of this relationship with high metallicities and large velocity widths are more likely to be sub-DLAs than DLA absorbers, perhaps implying that the sub-DLA absorbers are more representative of massive galaxies.

Key words: Quasars: absorption lines-ISM: abundances

1 INTRODUCTION

The chemical composition of galaxies provides important clues into galaxy formation and evolution. Absorption systems in QSO spectra provide an opportunity to study the interstellar medium (ISM) and therefore the chemical enrichment of galaxies. Damped Lyman- α (DLA) and sub-Damped Lyman- α (sub-DLA) absorbers are 2 classes of absorbers seen in the spectra of background QSOs. These high neutral hydrogen column density absorbers, particularly DLAs with $\log N_{\text{H I}} \geq 20.3$ and sub-DLAs with $19 \lesssim \log N_{\text{H I}} < 20.3$ (Péroux et al. 2001) are expected to contain the majority of the neutral gas in the universe, while the majority of the baryons are thought to lie in the highly ionized and diffuse Lyman- α forest clouds with $\log N_{\text{H I}} \lesssim 14$ (Petitjean et al. 1993). The DLA and sub-DLA systems are believed to be strongly related to galaxies at any redshift. Indeed, several DLA host galaxies have been con-

firmed through deep imaging at $z \lesssim 0.5$ eg; (Chen and Lanzetta 2003; Gharanfoli et al. 2006).

DLA systems have long been the preferred class of absorbers for chemical abundance studies. Observations by Dessauges-Zavadsky et al. (2003) of 12 sub-DLA absorbers at $1.8 < z < 4.3$ showed that these systems also contain metal line absorption features. Based on Fe II abundance measurements, Péroux et al. (2003a) suggested stronger metallicity evolution in sub-DLA systems than DLA systems. To date, very few observations have been made of $z < 1.5$ sub-DLAs. Redshifts $z < 1.5$ span 70% of the age of the universe (assuming a concordance cosmology of $\Omega_m = 0.3, \Omega_\Lambda = 0.7$). Clearly this redshift range is important to understanding the nature of sub-DLA systems and galactic chemical evolution as well.

Ionization effects can alter the abundances inferred for QSO absorbers. For DLAs, it is typically assumed that the ionization

corrections are small due to their large H I column densities that shield the cloud from ionizing photons. Dessauges-Zavadsky et al. (2003) showed that the ionization corrections for sub-DLA systems are also typically small, with < 0.2 dex corrections to most ions. It was also shown by Péroux et al. (2003b) that the contributions from DLAs to the neutral gas budget of the universe at $z > 3.5$ was lower than at $z < 3.5$ and that sub-DLAs harbored this remaining HI. Recently Péroux et al. (2006a); York et al. (2006); Kulkarni et al. (2007); Prochaska et al. (2006); Khare et al. (2006) have suggested that sub-DLAs may be more metal rich than DLAs, and may contribute significantly to the cosmic metal budget. Sub-DLAs have thus become a topic of much interest.

Many elements have been detected in QSO absorber systems, including C, N, O, Mg, Si, S, Ca, Ti, Cr, Mn, Fe, Ni, and Zn. Zn is often the preferred tracer of the gas-phase metallicity as it is relatively undepleted in the Galactic ISM, especially when the fraction of H in molecular form is low which is true in most DLAs. Zn also tracks the Fe abundance in Galactic stars, and the lines of Zn II $\lambda\lambda$ 2026, 2062 are relatively weak and typically unsaturated. These lines can also be covered with ground based spectroscopy over a wide range of redshifts, from $0.65 \lesssim z \lesssim 3.5$, which covers a large portion of the history of the universe. Relative abundances of refractory elements such as Cr and Fe relative to Zn also relate to the amount of extinction.

As galaxies mature, the ongoing processes associated with star formation such as stellar winds, supernovae explosions etc. expel metals into the interstellar medium. Over time, the interstellar metallicity is expected to reach a near solar value. Several models based on both analytical and semi-analytical calculations, as well as hydrodynamical simulations predict this increase to approximately solar values. Recent findings indicate that the $N_{\text{H I}}$ weighted mean metallicity (Z) of DLAs is well below solar ($\sim 0.1Z_{\odot}$ at $z = 2.0$ and $\sim 0.16Z_{\odot}$ at $z = 1$) and shows little if any evolution that is predicted by models (Kulkarni et al. 2005). Some lines of investigation are now suggesting that sub-DLAs may contain a significant portion of these “missing metals”, and may be more representative of typical massive spirals or ellipticals (Kulkarni et al. 2007; Khare et al. 2006). Wolfe (1993) claimed that the DLAs can be considered as progenitors to normal modern spirals, and argued that the line profiles suggest rotation curves (in absorption). Others however note that the absence of large galaxies in a number of searches for DLA host galaxies, suggesting that many are dwarf galaxies often with low impact parameters and lost in the light of the QSO (York et al. 1986; Hopkins, Rao, & Turnshek 2005). Kulkarni et al. (2007) show that based on available spectroscopic measurements, at $z \lesssim 1$ the contribution of sub-DLAs to the total metal budget may be several times greater than that of DLAs. For a constant dust-to-gas ratio, the dust obscuration bias is also expected to be less for sub-DLAs than for DLAs, therefore one might expect to be able to find metal rich sub-DLAs more frequently if dust obscuration effects are important.

Although difficult to constrain, it is generally acknowledged that there may be a significant ionization fraction in the sub-DLA systems, especially for systems with lower $N_{\text{H I}}$ (Péroux et al. 2003a; O’Meara et al. 2006). It has also been claimed that the sub-DLAs contain $\sim 15\%$ of the H atoms in the universe, and that they may be a distinct population of absorbers separated from the DLA absorbers (O’Meara et al. 2006). The H I column density distribution for QSO absorbers shows that systems with $19 \lesssim \log N_{\text{H I}} \lesssim 20.3$ are ~ 8 times more numerous than the higher column density classical damped Ly α systems, making sub-DLAs more readily available probes of neutral gas in the distant Universe.

In this paper we present high-resolution measurements of 7 sub-DLAs and 1 DLA taken with the Magellan Inamori Kyocera Echelle (MIKE) spectrograph on the 6.5m Clay telescope at Las Campanas observatory. The structure of this paper is as follows. In § 2, we discuss details of our observations and data reduction techniques. In § 3, column density determinations are discussed. § 4 gives information on the individual objects, while in § 5 we discuss the abundances of these absorbers, the Al III to Al II ratio, and ionization corrections, in § 6 we draw some general conclusions.

2 OBSERVATIONS AND DATA REDUCTION

The spectra presented here were obtained over 2 separate epochs, 2005 Sep. and 2006 February, respectively, with the 6.5m Magellan Clay telescope at Las Campanas Observatory. These objects were observed with the Magellan Inamori Kyocera Echelle spectrograph (MIKE) (Bernstein et al. 2003). This is a double sided spectrograph with both a blue and a red camera, providing for simultaneous wavelength coverage from $\sim 3340 \text{ \AA}$ to $\sim 9400 \text{ \AA}$. Targets were observed in multiple exposures of 1800 to 2700 sec to minimize cosmic ray defects. The seeing was typically $< 1''$, averaging $\sim 0.7''$. All of the target QSOs were observed with the $1'' \times 5''$ slit and the spectra were binned 2×3 (spatial by spectral) during readout. The resolving power of the MIKE spectrograph is $\sim 19,000$ and $\sim 25,000$ on the red and blue sides respectively with a $1'' \times 5''$ slit. Table 1 gives a summary of the observations.

These spectra were reduced using the MIKE pipeline reduction code in IDL developed by S. Burles, J. X. Prochaska, and R. Bernstein. Wavelengths were calibrated using a Th-Ar comparison lamp taken after each exposure. The MIKE software first bias subtracts from the overscan region and flat-fields the data, then sky-subtracts and extracts the spectral orders using the traces from flat field images. The pipeline calibration software also corrects for heliocentric velocities and converts the wavelengths to vacuum values. Each individual order was then extracted from the IDL structure created by the pipeline software and combined in IRAF using rejection parameters to reduce the effects of cosmic rays. These combined spectra were then normalized using a Legendre polynomial function to fit the continuum. Typically, these functions were of order five or less.

Our sample consists of 7 sub-DLAs and 1 DLA at $z < 1.5$, where there are few existing abundance measurements, including 3 absorbers with $z < 1.0$ where there are even fewer abundance measurements (Khare et al. 2004; Péroux et al. 2006a,b; Pettini et al. 2000). The objects from our sample were chosen partly because of strong lines of Mg II $\lambda\lambda$ 2796, 2803, or Fe II λ 2600 seen in SDSS spectra, or otherwise previously measured and given in Rao, Turnshek, & Nestor (2006). These sub-DLAs and the two observed in Péroux et al. (2006a,b) comprise all of high resolution observations of sub-DLAs at $z < 1.5$ to date. Four of the target QSOs in this sample were observed in the Sloan Digital Sky Survey (SDSS) and all have a known $N_{\text{H I}}$ from HST spectra. H I column densities were taken from Rao, Turnshek, & Nestor (2006) and references therein. We provide an appendix at the end of this paper showing the fits of the Lyman- α profiles from the UV spectra. Throughout this paper, the QSO names are given in J2000 coordinates.

Table 1. Summary of Observations

QSO J2000	Original or SDSS ID	RA	Dec	m_V	z_{em}	z_{abs}	$N_{H\ I}$ cm^{-2}	Exposure Time Sec	Epoch	Mg II Reference
Q0354-2724	Q0352-272	03:54:05.9	-27:24:25.7	17.9	2.823	1.4051	20.18 ± 0.15	10800	2005 Sep, 2006 Feb.	1
Q0826-2230	Q0823-223	08:26:01.5	-22:30:26.2	16.2	> 0.911	0.9110	19.04 ± 0.04	8627	2006 Feb.	2
Q1009-0026	SDSS J100930.46-002619.1	10:09:30.4	-00:26:19.1	17.4	1.244	0.8426	20.20 ± 0.06	8100	2006 Feb.	3
...	0.8866	19.48 ± 0.05	3
Q1010-0047	SDSS J101033.44-004724.5	10:10:33.4	-00:47:24.5	18.0	1.671	1.3270	19.81 ± 0.05	7191	2006 Feb.	3
Q1224+0037	SDSS J122414.29+003709.0	12:24:14.3	00:37:09.0	18.7	1.482	1.2346	20.88 ± 0.05	5400	2006 Feb.	3
...	1.2665	20.00 ± 0.07	3
Q2331+0038	SDSS J233121.81+003807.4	23:31:21.8	00:38:07.4	17.8	1.486	1.1414	20.00 ± 0.05	8000	2005 Sep	3

Notes – Emission redshifts are from the reference below, or if the target was observed in the SDSS, the emission redshift is from Schneider et al. (2005) Mg II References. – (1) Sargent, Steidel, & Boksenberg (1989), (2) Falomo (1990), (3) Nestor (2004)

Table 2. Rest-frame equivalent width measurements of key metal lines. Values and 1σ errors are in units of mÅ.

QSO	z_{abs}	Mg I	Mg II	Mg II	Al II	Al III	Al III	Si II	Si II	Ca II	Ca II	Cr II
		2852	2796	2803	1670	1854	1862	1526	1808	3933	3969	2056
Q0354-2724	1.4051	537 ± 9	2665 ± 14	2394 ± 10	$< 1114^a$	$< 412^a$	$< 607^a$	$< 1670^a$	64 ± 8
Q0826-2230	0.9110	123 ± 9	1280 ± 16	892 ± 15	...	< 9	< 9	...	< 10	22 ± 4	14 ± 4	< 5
Q1009-0026	0.8426	77 ± 14	713 ± 13	551 ± 13	...	77 ± 8	33 ± 6	< 10
Q1009-0026	0.8866	308 ± 22	1792 ± 16	1508 ± 18	...	146 ± 10	88 ± 13	...	< 12	103 ± 16	83 ± 14	< 5
Q1010-0047	1.3270	343 ± 18	2040 ± 14	1768 ± 15	883 ± 17	279 ± 9	141 ± 8	681 ± 21	44 ± 11	< 9
Q1224+0037	1.2346	212 ± 15	1086 ± 15	1032 ± 18	513 ± 17	159 ± 10	99 ± 9	477 ± 22	52 ± 7	47 ± 7
Q1224+0037	1.2665	188 ± 47	2181 ± 28	1876 ± 25	827 ± 15	84 ± 24	< 10	$< 1140^b$	< 12	< 9
Q2331+0038	1.1414	299 ± 19	2534 ± 43	2066 ± 47	424 ± 85	105 ± 50	52 ± 25	...	< 13	257 ± 23	141 ± 26	< 9
QSO	z_{abs}	Mn II	Mn II	Mn II	Fe II	Fe II	Fe II	Fe II	Fe II	Fe II	Zn II ^c	Zn II ^d
		2576	2594	2606	2260	2344	2374	2382	2586	2600	2026	2062
Q0354-2724	1.4051	126 ± 13	100 ± 10	75 ± 8	109 ± 9	1249 ± 18	739 ± 17	1657 ± 21	1143 ± 16	1715 ± 18	84 ± 10	68 ± 15
Q0826-2230	0.9110	< 5	< 5	< 5	< 4	161 ± 21	39 ± 15	444 ± 14	102 ± 10	353 ± 20	44 ± 8	26 ± 14
Q1009-0026	0.8426	27 ± 4	42 ± 6	< 8	31 ± 6	275 ± 6	179 ± 5	389 ± 4	265 ± 6	403 ± 5	< 13	< 10
Q1009-0026	0.8866	< 5	< 5	< 5	23 ± 4	625 ± 10	255 ± 10	1000 ± 12	568 ± 11	981 ± 18	41 ± 6	< 5
Q1010-0047	1.3270	< 15	< 15	< 15	0	905 ± 32	396 ± 24	1230 ± 14	741 ± 17	1269 ± 13	< 9	< 6
Q1224+0037	1.2346	< 29	< 29	< 29	< 40	632 ± 34	429 ± 35	758 ± 24	658 ± 29	827 ± 29	< 14	30 ± 7
Q1224+0037	1.2665	< 31	< 31	< 31	< 30	757 ± 28	271 ± 40	1206 ± 36	736 ± 65	1385 ± 27	< 13	< 9
Q2331+0038	1.1414	< 13	< 13	< 13	< 12	509 ± 13	324 ± 17	1206 ± 46	662 ± 36	1285 ± 36	29 ± 10	< 7

^aLines were blended with Lyman- α forest lines.

^bBlended with another feature.

^cThis line is a blend with Mg I λ 2026, although the Mg I contribution is judged to be insignificant in all cases.

^dAs this line is blended with the Cr II λ 2062 line, this value represents the total EW of the line.

3 DETERMINATION OF COLUMN DENSITIES

Column densities were determined from profile fitting with the package FITS6P (Welty et al. 1991), which has evolved from the code by Vidal-Madjar et al (1977). FITS6P iteratively minimizes the χ^2 value between the data and a theoretical Voigt profile that is convolved with the instrumental profile. The profile fit used multiple components, tailored to the individual system. For the central, core components, the Doppler parameters (b_{eff}) and radial velocities were determined from the weak and unsaturated lines, typically the Mg I λ 2852 line. For the weaker components at higher radial velocities the b_{eff} and component velocity values were determined from stronger transitions such as the Fe II $\lambda\lambda$ 2344, 2382 lines and the Mg II $\lambda\lambda$ 2796, 2803 lines. A set of b_{eff} and v values were thus determined that reasonably fit all of the lines observed in the system. The atomic data used in line identification and profile fitting are from Morton (2003).

In general, if a multiplet was observed, the lines were fit simultaneously until convergence. For all of the systems, the Fe II λ

2344, 2374, 2382 lines were fit simultaneously to determine a set of column densities that fit the spectra reasonably well. Similarly, the Mg II $\lambda\lambda$ 2796, 2803 lines were also fit together. The Zn II λ 2026 line is blended with a line of Mg I. The Mg I contribution to the line was estimated using the Mg I λ 2852 line, for which $f\lambda \sim 32$ times that of the λ Mg I 2026 line. The Zn II components were then allowed to vary while the Mg I components were held fixed. $N_{Cr\ II}$ was determined by simultaneously fitting the Cr II λ 2056 line and the blended Cr II + Zn II λ 2062 line, where the contribution from Zn II was estimated from the Zn II + Mg I λ 2026 line. See also Khare et al. (2004) for a discussion of the profile fitting scheme. In this paper we adopt the standard notation

$$[X/Y] = \log(N_X/N_{H\ I}) - \log(X/H)_{\odot}.$$

Solar system abundances have been adopted from Lodders (2003).

Using the package SPECIP, also developed by D.E. Welty, we determined equivalent widths as well as column densities via the apparent optical depth method (AOD) (Savage & Sembach 1996). We present the rest-frame equivalent widths (W_0) of the lines in

Table 4. The 1σ errors for the equivalent widths are given also and reflect both uncertainties in the continuum level and in the photon noise. If a certain line was not detected, the limiting equivalent width was determined from the local signal to noise ratio (S/N). Assuming a linear curve of growth, a 3σ upper limit was also placed on the column density.

4 DISCUSSION OF INDIVIDUAL OBJECTS

4.1 Q0354-2724 ($z_{em} = 2.823$)

This QSO ($M_V=17.9$) has a known sub-DLA with $\log N_{\text{H I}}=20.18$ at $z_{abs}=1.4051$ (Sargent, Steidel, & Boksenberg 1989; Rao, Turnshek, & Nestor 2006). We observed this target during both the 2005 Sep. and 2006 Feb. epochs for a total exposure time of 10800 sec. We detect strong absorption features of Mg I, Mg II, Cr II, Mn II, Fe II, and Zn II. The S/N varies from ~ 20 at $\sim 4900 \text{ \AA}$ to ~ 50 at $\sim 5700 \text{ \AA}$. Several lines of interest such as Al II $\lambda 1670$, Al III $\lambda\lambda 1854, 1862$ and Si II $\lambda 1808$ were inside the Lyman- α forest due to the relatively high redshift of the background QSO. Figure 1 shows velocity plots of several lines of interest for this system. There are no detectable components from the absorption system in any species outside the plotted range. Sargent et al. (1989) reported the existence of a C IV absorption system at $z_{abs} = 2.1442$ based on low-resolution ($\sim 6 \text{ \AA}$) observations. Based on these higher resolution spectra, we believe that this system was misidentified. There is a small feature at $\sim 350 \text{ km s}^{-1}$ of the Zn II $\lambda 2026$ line ($\lambda_{obs}=4878.7 \text{ \AA}$), as can be seen in figure 1, with $W_{obs}=67 \text{ m\AA}$. However, if this line is assumed to be the C IV $\lambda 1550$ line, then the $\lambda 1548$ line should be $\sim 4 \text{ \AA}$ blueward of the Zn II 2026 line. At the resolution of Sargent et al. (1989), the Zn II line from the $z_{abs} = 1.4051$ sub-DLA was likely confused for this C IV $\lambda 1548$ line. This feature is unidentified, it does not match any possible lines from the other known systems.

This system shows a complex velocity structure with a total of at least 8 components necessary to fit the observed profile. The total profile spans $\sim 360 \text{ km s}^{-1}$ (see § 5.4 for a more detailed discussion of how we derived the velocity width). We detect Zn II at S/N ~ 20 with $\log N_{\text{Zn II}}=12.73\pm 0.03$ for this sub-DLA giving a nearly solar abundance $[\text{Zn/H}]=-0.08$. The Mg I contribution to the blended Zn II + Mg I $\lambda 2026$ line was estimated from the Mg I $\lambda 2852$ line. In theory, if the Mg I $\lambda 2852$ line is saturated, which is rare but does occur occasionally for DLAs, the estimated contribution to the blended Zn II + Mg I $\lambda 2026$ line from the Mg I $\lambda 2852$ line could be lower than its true value. The EW of the Mg I $\lambda 2852$ line was $W_{rest} = 537 \text{ m\AA}$, which is below the 600 m\AA limit where the line begins to become significantly saturated (York et al. 2006). This system also shows moderate iron depletion with $[\text{Fe/Zn}]=-0.43$. Table 3 gives the results of the profile fitting analysis for each component.

4.2 Q0826-2230 ($z_{em} > 0.911$)

This is a BL Lac object. Due to the ambiguous emission redshift for this object, it is possible that this sub-DLA system is associated with the source itself. This object has a weak sub-DLA with $\log N_{\text{H I}}=19.04$ at $z=0.9110$ (Falomo 1990; Rao, Turnshek, & Nestor 2006). A total of 7 components were used in the theoretical profile. The total velocity width of the profile was $\sim 322 \text{ km s}^{-1}$. Figure 2 shows velocity plots for some of the lines of interest. We detect

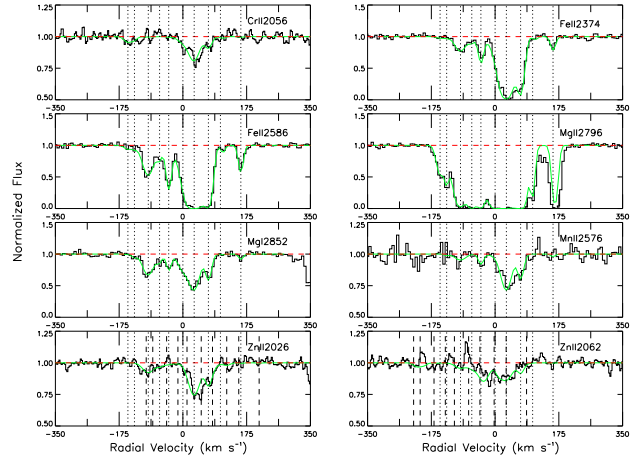


Figure 1. Velocity plots for several lines of interest in the $z = 1.4051$ system in the spectrum of Q0354-2724. The solid green line indicates the theoretical profile fit to the spectrum, and the dashed red line is the continuum level. The vertical dotted lines indicate the positions of the components that were used in the fit. In the case of the Zn II $\lambda\lambda 2026, 2062$ lines, the dashed vertical lines indicate the expected positions of the components of the Mg I ($\lambda 2026$) and Cr II ($\lambda 2062$) contributions respectively.

strong features of Mg II, Fe II, and Ca II. Mg I is also unambiguously detected, but the majority of the profile is contained in the component at $v = -65 \text{ km s}^{-1}$. We also detect Zn II $\lambda 2026$ and 2062 at S/N ~ 40 in the region, with the majority of the contribution from the $v = -65 \text{ km s}^{-1}$ component. There was a null detection of the Cr II $\lambda 2056$ line, which is the intrinsically strongest line available, so only a limit could be placed on $N_{\text{Cr II}}$.

This system has super-solar metallicity with $[\text{Zn/H}]=+0.68$ (see the appendix for a discussion of the H I values). The weaker Fe II $\lambda\lambda 2249, 2260$ lines were not detected in this system, but the Fe II $\lambda 2374$ line was unsaturated ($W_{rest}=39 \text{ m\AA}$, spread over 1 \AA) and an accurate column density could be determined. This system appears to have a high depletion with $[\text{Fe/Zn}]=-1.63$. The measured Ca II column density of $\log N_{\text{Ca II}}=11.75$ likely underestimates the true Ca column density because the ionization potential for Ca II is 11.868 eV is less than the ionization potential of H I. Table 4 gives the results of the Voigt profile fitting for each component.

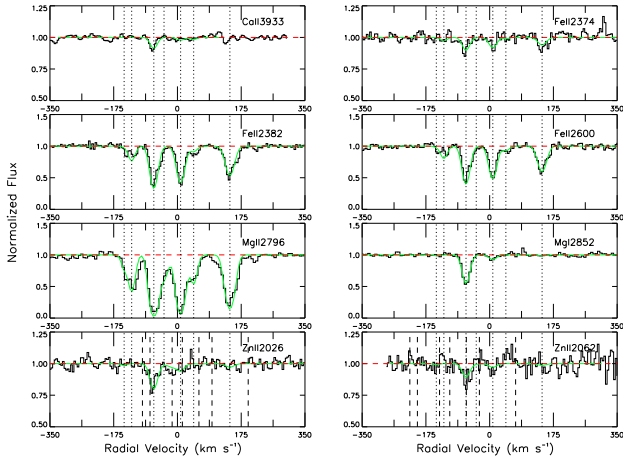
Grids of Cloudy models (Ferland et al. 1998) were constructed for this system which were tailored to fit the $N_{\text{H I}}$ and metallicity observed. The Al II $\lambda 1670$ line for this system was not in the wavelength section covered, and only limits could be placed on the Al III $\lambda\lambda 1854, 1862$ lines. We were however able to constrain the ionization parameter U based on the Mg II to Mg I ratio observed. Since the Mg II $\lambda\lambda$ lines were saturated, this ratio is only a lower limit, and the subsequent ionization corrections may be different. However, the Mg II lines were not optically thick at this resolution, and the true column density may not be much higher than the value given. The AOD column density also agrees very well with the profile fitting column density. Based on the model predictions, the ionization parameter is small and the ionization corrections for Zn are negligible ($<0.1 \text{ dex}$) for a large range of ionization parameters. See §5.3 for a more thorough account of the Cloudy modeling and ionization corrections.

Table 3. Column Densities for the $z = 1.4051$ absorber in Q0354-2724. Velocities and b_{eff} values are in units of km s^{-1} , and column densities are in units of cm^{-2} .

Vel	b_{eff}	Mg I	Mg II	Cr II	Mn II	Fe II	Zn II
-151	10.9	-	$(3.32 \pm 0.53)\text{E}+12$	$(2.07 \pm 0.68)\text{E}+12$	-	$(3.24 \pm 0.90)\text{E}+12$	-
-133	5.0	-	$(3.22 \pm 0.77)\text{E}+12$	-	-	-	-
-95	18.7	$(1.04 \pm 0.06)\text{E}+12$	$> 2.85\text{E}+13$	-	$(7.09 \pm 2.09)\text{E}+11$	$(4.89 \pm 0.20)\text{E}+13$	$(7.61 \pm 1.29)\text{E}+11$
-64	6.4	$(1.63 \pm 0.38)\text{E}+11$	$> 1.57\text{E}+14$	-	-	$(9.20 \pm 1.10)\text{E}+12$	-
-39	6.3	$(3.67 \pm 0.43)\text{E}+11$	$> 1.21\text{E}+14$	-	$(6.10 \pm 1.53)\text{E}+11$	$(5.66 \pm 0.39)\text{E}+13$	-
0	17.4	$(6.64 \pm 0.63)\text{E}+11$	$> 4.71\text{E}+13$	$(2.73 \pm 0.79)\text{E}+12$	-	$(4.62 \pm 0.31)\text{E}+13$	-
31	18.2	$(2.10 \pm 0.09)\text{E}+12$	$> 6.80\text{E}+13$	$(1.37 \pm 0.09)\text{E}+13$	$(4.80 \pm 0.27)\text{E}+12$	$(8.53 \pm 0.87)\text{E}+14$	$(3.85 \pm 0.16)\text{E}+12$
70	8.7	$(7.76 \pm 0.06)\text{E}+11$	$> 6.78\text{E}+14$	$(3.86 \pm 0.64)\text{E}+12$	$(1.85 \pm 0.19)\text{E}+12$	$(3.72 \pm 0.64)\text{E}+14$	$(8.16 \pm 1.09)\text{E}+11$
103	3.1	-	$> 8.11\text{E}+13$	-	-	$(4.13 \pm 0.89)\text{E}+12$	-
159	4.9	$(9.96 \pm 3.31)\text{E}+10$	$> 6.64\text{E}+13$	-	-	$(2.25 \pm 0.19)\text{E}+13$	-

Table 4. Same as table 3, but for the $z=0.9110$ absorber in Q0826-2230.

Vel	b_{eff}	Mg I	Mg II	Ca II	Fe II	Zn II
-146	9.4	-	$(9.77 \pm 1.72)\text{E}+11$	-	-	-
-126	11.6	-	$(4.22 \pm 0.28)\text{E}+12$	-	$(2.94 \pm 0.74)\text{E}+12$	-
-65	13.1	$(1.08 \pm 0.05)\text{E}+12$	$> 1.94\text{E}+13$	$(3.37 \pm 0.19)\text{E}+11$	$(1.37 \pm 0.10)\text{E}+13$	$(1.82 \pm 0.19)\text{E}+12$
-37	14.7	-	$(2.86 \pm 0.26)\text{E}+12$	-	-	-
9	13.8	$(1.42 \pm 0.30)\text{E}+11$	$> 1.51\text{E}+13$	$(8.63 \pm 1.83)\text{E}+10$	$(1.14 \pm 0.09)\text{E}+13$	$(4.26 \pm 1.74)\text{E}+11$
45	12.0	-	$(3.07 \pm 0.23)\text{E}+12$	$(5.38 \pm 1.71)\text{E}+10$	-	-
144	15.4	-	$> 1.21\text{E}+13$	$(8.00 \pm 1.92)\text{E}+10$	$(8.98 \pm 0.90)\text{E}+12$	-

**Figure 2.** The same as fig.1, but for the $z=0.9110$ system in the spectrum of Q0826-2230

4.3 Q1009-0026 ($z_{em} = 1.244$)

This system has two confirmed sub-DLAs with $\log N_{\text{H I}} = 20.20$ at $z = 0.8426$ (system A) and $\log N_{\text{H I}} = 19.48$ at $z = 0.8866$ (system B) (Nestor 2004; Rao, Turnshek, & Nestor 2006). System A shows a relatively simple velocity structure with only 4 components needed to fit the observed profile. The profile for system A spans a total of $\sim 94 \text{ km s}^{-1}$. For this system, the Al II line was below the wavelength region covered by the spectrograph, but the Al III $\lambda\lambda 1854, 1862$ lines were observed although the dominant species is likely Al II. This system also shows fairly strong Mn II $\lambda\lambda 2576, 2594, 2606$ lines. We did not detect any Zn II $\lambda\lambda 2026$

lines with $S/N \sim 20$ in the region, so we give the metallicity as an upper limit. This system has a low metallicity, with $[\text{Zn}/\text{H}] < -0.98$, $[\text{Fe}/\text{H}] = -1.28$, and $[\text{Mn}/\text{H}] = -1.44$ although both Mn and Fe are often depleted in the Galaxy.

System B shows a more complicated velocity structure with 7 components needed to fit the profile. This system has a larger velocity width, spanning $\sim 334 \text{ km s}^{-1}$. Again, the Al II $\lambda 1670$ line was not in the wavelength region, but Al III $\lambda\lambda 1854, 1862$ lines were detected. A $S/N \sim 25$ was reached in the region of Zn II $\lambda 2026$ which was detected at $\sim 5\sigma$ with an equivalent width $W_{rest} = 41 \text{ mÅ}$. Profile fitting of the line gives $\log N_{\text{Zn II}} = 12.36$ and $[\text{Zn}/\text{H}] = +0.25$. We were able to constrain the ionization parameter for this system to be $\log U = -3.70$ based on the observed Al III to Fe II ratio (see § 5.3 for a more detailed discussion of the method). The Ca II $\lambda\lambda 3933, 3969$ lines were also detected in this system with $\log N_{\text{Ca II}} = 12.26$. Mn was not detected in this system with $[\text{Mn}/\text{Fe}] < -1.24$. Tables 5 and 6 show the results of the Voigt profile decomposition for systems A and B respectively.

4.4 Q1010-0047 ($z_{em} = 1.671$)

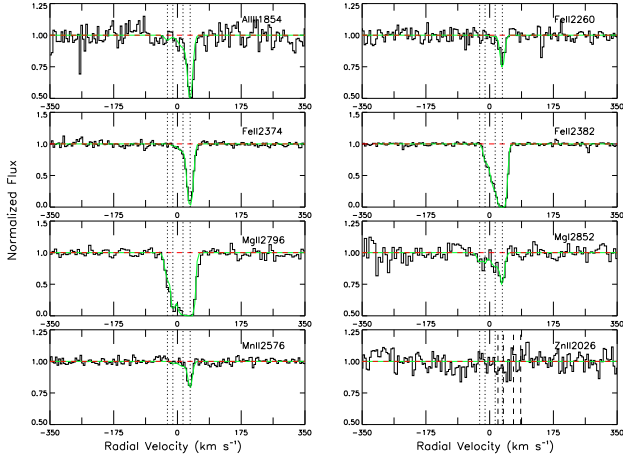
This system has a confirmed sub-DLA with $\log N_{\text{H I}} = 19.81$ at $z = 1.3270$ (Nestor 2004; Rao, Turnshek, & Nestor 2006). This system was fit with a 8 component model. The profile spanned $\sim 308 \text{ km s}^{-1}$ in total. We detect strong lines of Mg II, Al II, Al III, and Fe II in this system but no detection of Zn II $\lambda 2026$ in the region with $S/N \sim 30$. Table 7 shows the results of the profile fitting for each component. From the 3σ limiting equivalent width of $W_{rest} = 9 \text{ mÅ}$, this system has $\log N_{\text{Zn II}} < 11.67$ and $[\text{Zn}/\text{H}] < -0.75$. We detect strong Si II $\lambda\lambda 1526, 1808$ lines with $\log N_{\text{Si II}} = 15.02$. This system also shows apparent α -enhancement with $[\text{Si}/\text{Fe}] = 0.42$. Although depletion may be important, the metallicities based on Si

Table 5. Same as table 3, but for the $z=0.8426$ absorber in Q1009-0026.

Vel	b_{eff}	Mg I	Mg II	Al III	Mn II	Fe II
-28	8.7	-	$(1.95 \pm 0.21)E+12$	-	-	-
-13	5.6	-	$(5.74 \pm 0.66)E+12$	-	-	$(1.53 \pm 0.32)E+12$
15	16.7	$(2.60 \pm 0.64)E+11$	$> 2.83E+13$	$(1.16 \pm 0.28)E+12$	$(4.89 \pm 1.11)E+11$	-
35	7.2	$(2.73 \pm 0.50)E+11$	$> 1.65E+14$	$(4.20 \pm 0.33)E+12$	$(1.34 \pm 0.08)E+12$	$(2.47 \pm 0.23)E+14$

Table 6. Same as table 3, but for the $z=0.8866$ absorber in Q1009-0026.

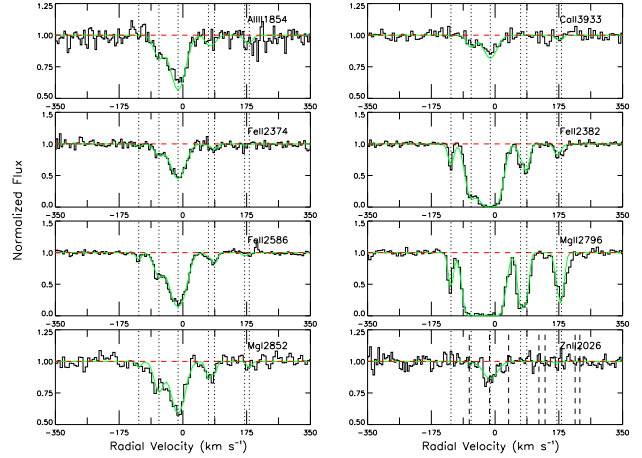
Vel	b_{eff}	Mg I	Mg II	Al III	Ca II	Fe II	Zn II
-121	4.6	-	$(4.47 \pm 0.49)E+12$	-	-	$(4.69 \pm 0.57)E+12$	-
-66	15.6	$(6.22 \pm 0.65)E+11$	$> 7.77E+13$	$(2.51 \pm 0.24)E+12$	$(4.58 \pm 0.65)E+11$	$(3.22 \pm 0.11)E+13$	-
-13	23.9	$(1.72 \pm 0.09)E+12$	$> 2.02E+14$	$(9.99 \pm 0.36)E+12$	$(1.35 \pm 0.08)E+12$	$(3.31 \pm 0.31)E+14$	$(2.28 \pm 0.26)E+12$
70	5.2	$(1.99 \pm 0.48)E+11$	$> 2.49E+13$	$(6.71 \pm 2.13)E+11$	-	$(2.40 \pm 0.52)E+12$	-
87	3.6	-	$> 1.32E+13$	-	-	$(8.16 \pm 0.79)E+12$	-
169	4.4	-	$(1.99 \pm 0.31)E+12$	-	-	$(1.93 \pm 0.57)E+12$	-
182	5.1	-	$(9.47 \pm 1.23)E+12$	-	-	-	-

**Figure 3.** The same as fig.1, but for the $z=0.8426$ system in the spectrum of Q1009-0026

and Fe are $[Si/H]=-0.33$ and $[Fe/H]=-0.75$. As there were detections of both Al II and Al III in this system, we were able to constrain the ionization parameter U for this system to be $\log U \lesssim -4.15$. See § 5.4 and § 5.5 for a more complete discussion of the Cloudy modeling and ionization corrections. Figure 5 gives velocity plots for some of the lines of interest in this system. The feature at ~ -300 km s^{-1} in the plot of Al III λ 1862 is unidentified. There are several other systems seen in the spectrum of this QSO, but no known lines match the observed wavelength of this feature.

4.5 Q1224+0037 ($z_{em} = 1.482$)

This QSO has a DLA with $\log N_{\text{H I}}=20.88$ at $z_{abs} = 1.2346$ (system A) and a sub-DLA with $\log N_{\text{H I}}=20.00$ at $z_{abs} = 1.2665$ (system B) (Nestor 2004; Rao, Turnshek, & Nestor 2006). System A shows a relatively simple velocity structure with 5 components needed to fit the observed profile. The profile spans ~ 129 km s^{-1} . Strong Mg II $\lambda\lambda$ 2796, 2803 and Fe II $\lambda\lambda$ 2344, 2374, 2382 lines

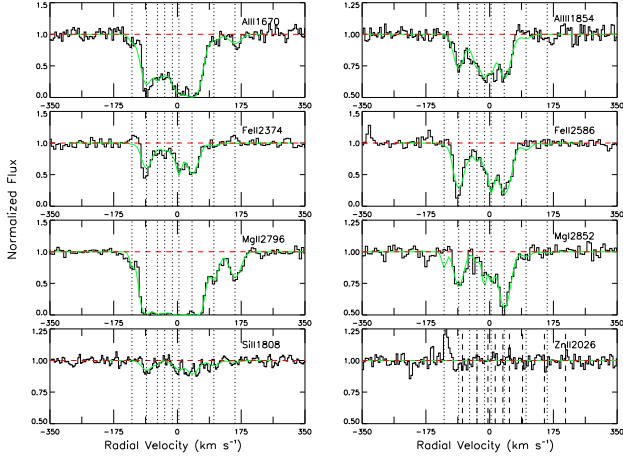
**Figure 4.** The same as fig.1, but for the $z=0.8866$ system in the spectrum of Q1009-0026

were detected in this system. Zn II $\lambda\lambda$ 2026 or 2062 lines were not, however, detected in this system at $S/N \sim 18$ in the region, with $[Zn/H] < -1.62$. Strong Al II λ 1670 absorption was seen in this system along with weaker Al III $\lambda\lambda$ 1854, 1862 lines. Strong Si II $\lambda\lambda$ 1526, 1808 were also seen with $\log N_{\text{Si II}}=15.10$. The weaker Fe II $\lambda\lambda$ 2249, 2260 lines were not detected so only a lower limit could be placed on $\log N_{\text{Fe II}} > 15.11$ based on the saturated Fe II $\lambda\lambda$ 2344, 2374, 2382 lines. The metallicities based on Si, Fe, and Zn are $[Si/H]=-1.32$ $[Zn/H] < -1.62$, and $[Fe/H] > -1.24$. The Cr II $\lambda\lambda$ 2056, 2062 lines were observed in this system with rest frame equivalent widths of 47 and 30 mÅ respectively. The Zn II λ 2026 line was not however detected. Table 8 gives the results of the profile fitting for each of the components. Figure 6 shows velocity plots for several of the lines of interest in this system.

System B shows a more complicated velocity structure with a total of 8 components needed to fit the observed profile. This system also shows a larger velocity width of ~ 253 km s^{-1} . Mg II $\lambda\lambda$ 2796, 2803 lines were detected along with strong Fe II $\lambda\lambda$

Table 7. Same as table 3, but for the $z = 1.3270$ absorber in Q1010-0047.

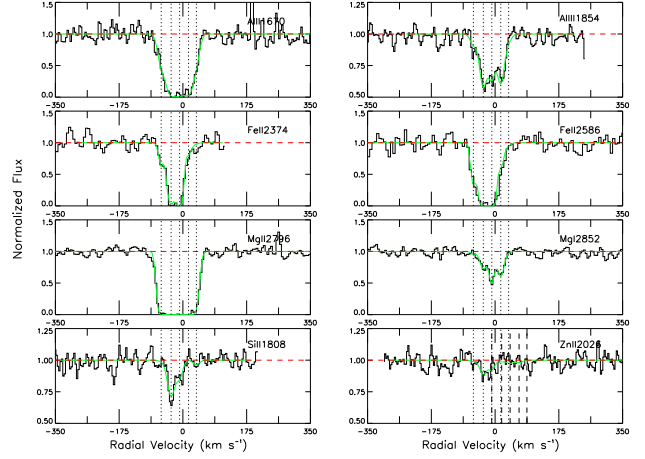
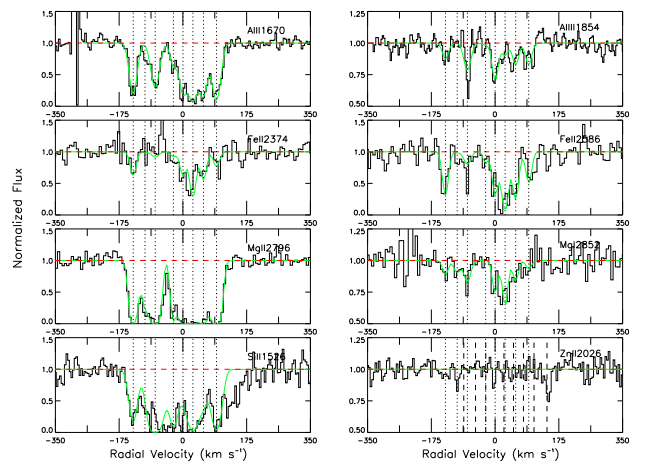
Vel	b_{eff}	Mg I	Mg II	Al II	Al III	Si II	Fe II
-125	4.9	$(1.53 \pm 0.46)E+11$	$(8.63 \pm 1.59)E+11$	-	-	-	-
-85	16.3	$(7.44 \pm 0.73)E+11$	$> 3.48E+13$	$> 7.87E+12$	$(4.06 \pm 0.37)E+12$	$(2.82 \pm 0.47)E+14$	$(8.72 \pm 0.47)E+13$
-55	4.2	-	$> 4.74E+14$	$> 5.45E+12$	-	-	$(6.21 \pm 1.61)E+12$
-35	10.2	-	$> 2.02E+13$	$> 3.55E+12$	$(2.91 \pm 0.37)E+12$	-	$(1.65 \pm 0.18)E+13$
-14	3.9	$(3.58 \pm 0.62)E+11$	$> 4.21E+14$	$> 4.96E+12$	$(2.97 \pm 0.48)E+12$	-	$(1.56 \pm 0.26)E+13$
4	7.0	-	$> 3.47E+14$	$> 1.64E+13$	$(2.83 \pm 0.37)E+12$	$(1.66 \pm 0.41)E+14$	$(7.19 \pm 0.73)E+13$
40	19.9	$(1.62 \pm 0.10)E+12$	$> 1.81E+14$	$> 3.66E+13$	$(6.41 \pm 0.43)E+12$	$(4.57 \pm 0.51)E+14$	$(1.31 \pm 0.06)E+14$
100	15.6	-	$(3.83 \pm 0.26)E+12$	-	-	$(1.43 \pm 0.43)E+14$	$(7.43 \pm 1.43)E+12$
158	19.2	-	$(4.18 \pm 0.26)E+12$	-	-	-	-

**Figure 5.** The same as fig.1, but for the $z=1.3270$ system in the spectrum of Q1010+0047

2344, 2374, 2382 lines. This system also has a saturated Al II λ 1670 line with $\log N_{\text{Al II}} > 13.72$ and unsaturated Al III $\lambda\lambda$ 1854, 1862 lines that were fit simultaneously to give $\log N_{\text{Al III}} = 12.98$. The Si II λ 1526 line appears to be blended with another feature, as can be seen in figure 7. We therefore give an upper limit on the column density $N_{\text{Si II}} < 14.30$ based on the non-detection of the Si II λ 1808 line. There also may be some blending near the $v = -104 \text{ km s}^{-1}$ component in the Fe II λ 2600 due to the lack of this component in the other Fe II lines. No Zn II $\lambda\lambda$ 2026, 2062 lines were seen with $S/N \sim 20$ in the region. Table 9 gives the results of the profile fitting for system B. Velocity plots of lines of interest are shown in figure 7.

4.6 Q2331+0038 ($z_{em} = 1.714$)

This QSO harbors a sub-DLA with $\log N_{\text{H I}} = 20.00$ (Nestor 2004; Rao, Turnshek, & Nestor 2006). This system exhibits a complex velocity structure needing 9 components to fit the profile. The total profile spans more than 558 km s^{-1} . The 2 components at $v = -255$ and $v = -204 \text{ km s}^{-1}$ appear mainly in the strong Mg II $\lambda\lambda$ 2796, 2803 and the stronger Fe II transitions. We detect Zn II λ 2026 in this system at $\sim 3\sigma$ with $\log N_{\text{Zn II}} = 12.12$ and $[\text{Zn}/\text{H}] = -0.51$. The Zn II is found solely in the $v = 45 \text{ km s}^{-1}$ component, which is the strongest component in Mg I λ 2852 and the Fe II lines. The contribution of Mg I to the blended Zn II + Mg I λ 2026 line is small, $W_0 \sim 300 \text{ mÅ}$ for the Mg I λ 2852

**Figure 6.** The same as fig.1, but for the $z=1.2346$ system in the spectrum of Q1224+0037**Figure 7.** The same as fig.1, but for the $z=1.2665$ system in the spectrum of Q1224+0037

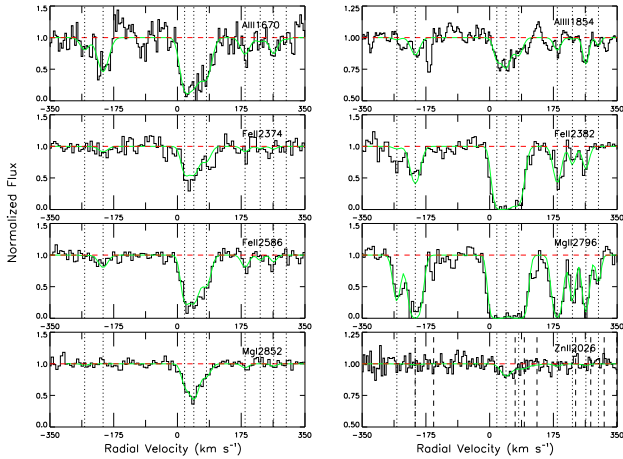
line, well below the level discussed in § 4.1 where saturation may become important. There appears to be an interloper at $v \sim -170 \text{ km s}^{-1}$ of the Al III λ 1854 line. Table 10 summarizes the results of the profile fitting analysis for this system, and figure 10 shows the velocity plots for several lines of interest.

Table 8. Same as table 3, but for the $z=1.2346$ DLA in Q1224+0037.

Vel	b_{eff}	Mg I	Mg II	Al II	Al III	Si II	Cr II	Fe II
-60	8.2	-	$(5.85 \pm 1.12)E+13$	$>2.14E+12$	$(7.01 \pm 2.02)E+11$	-	-	$(3.69 \pm 1.12)E+13$
-32	10.8	$(5.14 \pm 0.64)E+11$	$>9.68E+13$	$>2.04E+13$	$(4.97 \pm 0.34)E+12$	$(8.45 \pm 0.94)E+14$	$(9.27 \pm 1.40)E+12$	$>3.69E+14$
-9	8.0	$(8.93 \pm 0.84)E+11$	$>3.73E+14$	$>1.50E+13$	$(3.29 \pm 0.29)E+12$	$(3.19 \pm 0.75)E+14$	$(3.77 \pm 1.19)E+12$	$>8.51E+14$
16	10.4	$(7.63 \pm 0.74)E+11$	$>1.82E+14$	$>2.14E+12$	$(4.44 \pm 0.32)E+12$	$(9.16 \pm 2.85)E+13$	-	-
37	8.2	-	$(8.12 \pm 1.24)E+12$	$>1.69E+12$	-	-	-	-

Table 9. Same as table 3, but for the $z=1.2665$ absorber in Q1224+0037.

Vel	b_{eff}	Mg I	Mg II	Al II	Al III	Fe II
-136	7.8	-	$>8.95E+13$	$>7.11E+12$	$(1.00 \pm 0.28)E+12$	$(4.95 \pm 0.94)E+13$
-104	10.4	-	$>6.62E+12$	$>6.46E+11$	-	-
-76	10.5	-	$>1.13E+14$	$>4.21E+12$	$(2.15 \pm 0.33)E+12$	$(1.07 \pm 0.34)E+13$
-26	5.1	-	$>3.48E+13$	$>1.49E+12$	-	-
0	8.1	$(3.96 \pm 0.99)E+11$	$>1.23E+14$	$>7.16E+12$	$(2.75 \pm 0.36)E+12$	$(5.01 \pm 0.96)E+13$
28	7.9	$(5.93 \pm 1.14)E+11$	$>1.90E+14$	-	$(7.72 \pm 2.71)E+11$	$(1.45 \pm 0.30)E+14$
57	7.9	-	$>8.54E+13$	$>1.06E+13$	$(1.47 \pm 0.30)E+12$	$(6.15 \pm 1.17)E+13$
92	8.1	-	$>3.12E+14$	$>2.09E+13$	$(1.45 \pm 0.30)E+12$	$(2.82 \pm 0.56)E+13$

**Figure 8.** The same as fig.1, but for the $z=1.1414$ system in the spectrum of Q2331+0038

5 RESULTS

5.1 Total Column Densities

In table 11 we summarize the total column densities for the different species for all of the absorbers in this sample. Cells with entries “...” have undetermined column densities because of lack of wavelength coverage, being blended with Lyman- α forest clouds, blending with atmospheric absorption bands, or very high noise levels due to the inefficiencies of the spectrograph at the wavelength extremes. Several systems showed significant saturation in the lines of Mg II, Al II, and Fe II so the values listed are given as lower limits. In general the column densities derived from the AOD method are slightly less than the ones derived from the profile fitting analysis for unsaturated lines, and differ by up to ~ 0.8 dex in the saturated Mg II lines. For stronger absorption lines, Savage & Sembach (1991) showed that the instrumental res-

olution affects the column density derived via the apparent optical depth method. For fully resolved profiles, Savage & Sembach (1991) showed that the apparent column density was very close to the “true” column density, whereas for unresolved profiles, even in moderately strong lines there was significant departure from the “true” column density that indicate hidden absorption in the profile. At the ~ 20 km s $^{-1}$ resolution obtained with the settings used on MIKE, there are likely unresolved components and therefore departures from the true column density by those given from the apparent optical depth method.

In table 12 we give the metallicity of these systems from profile fitting, and also the abundance ratio [Fe/Zn], which is often taken as an indicator of dust depletion. We also give [Si/Fe], [Ca/Fe], [Cr/Fe], and [Mn/Fe] for these systems. The ratios of column densities of the adjacent ions Mg II / Mg I and Al II / Al III are given, as well as Mg II / Al III and Fe II / Al III. For every absorber in this sample, there is an under-abundance of Mn relative to Fe. This could be a sign of the even-odd effect, although dust depletion can confuse this. There also appears to be a trend similar to that of DLA systems of higher depletion of Fe with increasing metallicity (Prochaska & Wolfe 2002; Ledoux, Petitjean, & Srianand 2003; Herbert-Fort et al. 2006; Meiring et al. 2006) seen in these sub-DLA systems. Only the $z = 1.3270$ sub-DLA in Q1010-0047 shows any signs of α -enhancement with [Si/Fe]=+0.42 although dust depletion is also a possibility. It is also worth noting that this system shows a low metallicity based on Zn ([Zn/H]<-0.75), but higher [Fe/H] and [Si/H]. This would suggest that, at least for this system, comparing Si and Zn metallicities may give vastly different results. This type of non-standard abundance may not be unexpected, the zones sampled by the background QSOs are small due to the small size of the QSO beam, and multiple regions probed within a galaxy can show up as different components. Similarly, contamination by a small number of supernovae may produce odd abundance patterns due to the relatively young, unmixed gas.

Table 10. Same as table 3, but for the $z=1.1414$ absorber in Q2331+0038.

Vel	b_{eff}	Mg I	Mg II	Al II	Al III	Fe II	Zn II
-255	10.7	-	(7.09 \pm 0.76)E+12	-	-	-	-
-204	15.1	-	>4.43E+13	(3.76 \pm 0.67)E+12	(1.61 \pm 0.34)E+12	(1.42 \pm 0.22)E+13	-
20	10.4	(5.77 \pm 0.83)E+11	>2.62E+14	>8.24E+12	(1.41 \pm 0.31)E+12	(6.48 \pm 0.75)E+13	-
45	16.5	(1.93 \pm 0.13)E+12	>1.93E+13	>7.31E+12	(3.21 \pm 0.42)E+12	(1.02 \pm 0.09)E+14	(1.32 \pm 0.32)E+12
80	13.8	(4.50 \pm 0.70)E+11	>2.21E+14	>4.74E+12	(1.52 \pm 0.33)E+12	(4.03 \pm 0.39)E+13	-
186	11.4	-	>3.44E+13	(1.26 \pm 0.40)E+12	(9.27 \pm 2.95)E+11	(1.16 \pm 0.20)E+13	-
227	7.2	-	>6.65E+12	-	-	-	-
264	8.3	-	>1.35E+13	(1.13 \pm 0.41)E+12	(1.74 \pm 0.31)E+12	(5.12 \pm 0.16)E+12	-
299	5.0	-	(2.54 \pm 0.49)E+12	-	-	-	-

Table 11. Total column densities from the absorbers in this sample.

QSO	z_{abs}	$\log N_{H\text{ I}}$ cm^{-2}	$\log N_{Mg\text{ I}}$ cm^{-2}	$\log N_{Mg\text{ II}}$ cm^{-2}	$\log N_{Al\text{ I}}$ cm^{-2}	$\log N_{Al\text{ II}}$ cm^{-2}	$\log N_{Si\text{ II}}$ cm^{-2}	$\log N_{Ca\text{ II}}$ cm^{-2}	$\log N_{Cr\text{ II}}$ cm^{-2}	$\log N_{Mn\text{ II}}$ cm^{-2}	$\log N_{Fe\text{ II}}$ cm^{-2}	$\log N_{Zn\text{ II}}$ cm^{-2}
Q0354-2724	1.4051	20.18 \pm 0.15	12.72 \pm 0.02	>15.08	13.35 \pm 0.06	12.90 \pm 0.06	15.15 \pm 0.05	12.73 \pm 0.03
AOD			12.70 \pm 0.01	>14.39					13.25 \pm 0.04	12.82 \pm 0.03	15.03 \pm 0.01	12.72 \pm 0.03
Q0826-2230	0.9110	19.04 \pm 0.04	12.09 \pm 0.03	>13.76	...	<11.72	<14.22	11.75 \pm 0.06	<12.11	<11.37	13.57 \pm 0.04	12.35 \pm 0.07
AOD			12.06 \pm 0.02	>13.71				11.42 \pm 0.04			13.43 \pm 0.12	12.41 \pm 0.05
Q1009-0026	0.8426	20.20 \pm 0.06	11.73 \pm 0.09	>14.30	...	12.73 \pm 0.05	<12.41	12.26 \pm 0.05	14.39 \pm 0.04	<11.85
AOD			11.80 \pm 0.05	>13.87		12.74 \pm 0.03				12.28 \pm 0.04	14.37 \pm 0.03	
Q1009-0026	0.8866	19.48 \pm 0.05	12.41 \pm 0.04	>14.52	...	13.12 \pm 0.03	<14.26	12.26 \pm 0.04	<12.11	<11.37	14.58 \pm 0.04	12.36 \pm 0.04
AOD			12.43 \pm 0.02	>14.32		13.00 \pm 0.02		12.10 \pm 0.04			14.33 \pm 0.06	12.38 \pm 0.04
Q1010-0047	1.3270	19.81 \pm 0.05	12.46 \pm 0.02	>15.17	>13.87	13.28 \pm 0.02	15.02 \pm 0.02	...	<12.37	<11.85	14.53 \pm 0.03	<11.69
AOD			12.49 \pm 0.02	>14.26	>13.72	13.29 \pm 0.02	14.86 \pm 0.15				14.50 \pm 0.02	
Q1224+0037	1.2346	20.88 \pm 0.05	12.34 \pm 0.04	>14.86	>13.62	13.13 \pm 0.04	15.10 \pm 0.07	...	13.12 \pm 0.09	<12.14	>15.11	<11.89
AOD			12.31 \pm 0.03	>14.30	>13.59	13.07 \pm 0.03	15.01 \pm 0.05		13.14 \pm 0.05		>14.99	
Q1224+0037	1.2665	20.00 \pm 0.07	12.00 \pm 0.10	>14.97	>13.72	12.98 \pm 0.08	<14.30	...	<12.37	<12.16	14.54 \pm 0.09	<11.85
AOD			12.21 \pm 0.08	>14.25	>13.56	12.74 \pm 0.14					14.36 \pm 0.04	
Q2331+0038	1.1414	20.00 \pm 0.05	12.48 \pm 0.05	>14.79	>13.42	13.02 \pm 0.09	<14.33	...	<12.37	<11.79	14.38 \pm 0.03	12.12 \pm 0.11
AOD			12.47 \pm 0.03	>14.39	>13.33	12.86 \pm 0.14					14.44 \pm 0.05	12.22 \pm 0.09

5.2 The Al III to Al II Ratio and Ionized Gas

Based on the ionization potentials of the Al^0 and Al^+ ions (5.99 and 18.83 eV respectively), one would expect that the majority of the Al seen in DLA and sub-DLA systems would be in the first ionization stage (Al^+), and that the second ionization stage (Al^{++}) would be all but absent due to the shielding of photons with energies greater than the ionization potential of hydrogen (13.6 eV). The Al III $\lambda\lambda$ 1854, 1862 lines are nonetheless often seen in DLA spectra although the majority is always in Al II. As is seen in most DLAs, the Al III $\lambda\lambda$ 1854, 1862 lines of the systems studied here have very similar component structures to the lower ionization state lines such as Fe II, Mg II. Higher ionization state transitions such as C IV or S IV often show very different component structures than the low ion transitions, implying pockets of local, highly ionized gas within the DLA/sub-DLA, or possibly galactic halos. The similar structure of the Al III and low ion profiles suggests that these systems are physically connected.

The Al III / Al II ratios have in the past been used to investigate the ionization states of QSO absorbers. Vladilo et al. (2001) observed an anti-correlation between the Al III / Al II ratio and $N_{H\text{ I}}$ based on a sample of 20 DLAs, where the Al II column density was estimated from Si II in most cases. They suggested that the higher $N_{H\text{ I}}$ systems also had lesser degrees of ionization. It should be noted however that there may be issues with using Si as a surrogate for Al (Barker et al. 1984). Dessauges-Zavadsky et al. (2003) noted however that when the data were extended into the column density region of sub-DLAs, the trend seemed to disappear. In figure 9, we show the Al III / Al II ratio for the absorbers from this

work, Dessauges-Zavadsky et al. (2003), and Vladilo et al. (2001). As can be seen from the original data of Vladilo et al. (2001) (blue squares, black diamonds, and purple triangle), the before mentioned trend does seem to hold for these data. It can also be seen in figure 9 that the $z > 1.8$ sub-DLAs of Dessauges-Zavadsky et al. (2003) and the $z < 1.5$ absorbers seen here show similar Al III / Al II ratios, suggesting little evolution of this parameter although the sample sizes are still small. With one exception of 30 cases in figure 9, which covers $19 < \log N_{H\text{ I}} < 21.7$, $N_{Al\text{ III}}/N_{Al\text{ II}} \lesssim -0.25$. Models from Petitjean, Rauch, & Carswell (1994) also showed little change in the Al III/Al II ratio especially when $17 \lesssim \log N_{H\text{ I}} \lesssim 20$. Similarly, York et al. (2006) found the ratio to change very little over a wide range of reddenings corresponding to the same range in $N_{H\text{ I}}$.

5.3 Cloudy Modeling and Ionization Corrections

It is generally assumed for DLAs that the gas has a very low ionization fraction, and that most metal ions are mainly in the first ionization state. This is because of the self-shielding of photons with $h\nu > 13.6$ eV due to the large cross section for ionization of H at these energies. Therefore, the abundances reported for QSO absorbers are typically derived from lines originating from ions and may not reflect the true abundances. The ionization correction factor, defined here as

$$\epsilon = [X/H]_{\text{total}} - [X^+/H^0]$$

where the total column densities include contributions from all ionization stages, has been investigated for DLAs by several groups

Table 12. Abundances for the absorbers in this sample.

QSO	z_{abs}	[Zn/H]	[Fe/H]	[Fe/Zn]	[Si/Fe]	[Ca/Fe]	[Cr/Fe]	[Mn/Fe]	Al III / Al II	Mg II / Mg I	Mg II / Al III	Fe II / Al III
$[X/Y]_{\odot}$		-7.37	-4.53	+2.85	+0.07	-1.13	-1.82	-1.97				
Q0354-2724	1.4051	-0.08 ± 0.16	-0.50 ± 0.16	-0.43 ± 0.06	0.02 ± 0.07	-0.35 ± 0.08	...	> 2.36
Q0826-2230	0.9110	$+0.68 \pm 0.08$	-0.94 ± 0.06	-1.63 ± 0.08	< 0.58	-0.69 ± 0.07	$< +0.36$	< -0.23	...	> 1.67	> 2.04	> 1.85
Q1009-0026	0.8426	< -0.98	-1.28 ± 0.07	> -0.31	< -0.16	-0.16 ± 0.06	...	> 2.57	> 1.57	1.66 ± 0.06
...	0.8866	$+0.25 \pm 0.06$	-0.37 ± 0.06	-0.63 ± 0.06	< -0.39	-1.19 ± 0.06	< -0.65	< -1.24	...	> 2.11	> 1.40	1.46 ± 0.05
Q1010-0047	1.3270	< -0.75	-0.75 ± 0.06	> 0.01	0.42 ± 0.07	...	< -0.34	< -0.71	< -0.71	> 2.71	> 1.69	1.25 ± 0.05
Q1224+0037	1.2346	< -1.62	> -1.24	> 0.37	< -0.08	...	< -0.17	...	< -0.49	> 2.52	> 1.73	> 1.98
...	1.2665	< -0.78	-0.93 ± 0.11	> -0.16	< -0.31	...	< -0.35	< -0.41	< -0.74	> 2.97	> 1.99	1.56 ± 0.12
Q2331+0038	1.1414	-0.51 ± 0.12	-1.09 ± 0.06	-0.59 ± 0.11	< -0.12	...	< -0.19	< -0.62	< -0.40	> 2.31	> 1.77	1.36 ± 0.09

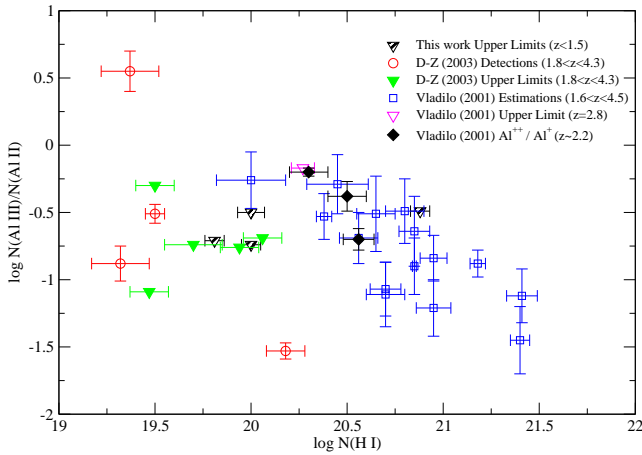


Figure 9. The Al III / Al II ratio for the absorbers in this sample (striped triangles), Dessauges-Zavadsky et al. (2003) (solid triangles), and Vladilo et al. (2001) (blue squares, purple triangle, and black diamonds). For the Vladilo et al. (2001) systems, the blue squares represent systems where Al II was estimated from Si II, the black diamond points are for systems with true Al III / Al II values, and the purple triangle is an upper limit based on Al III / Al II. All of the absorbers from this work with Al II measurements showed significant saturation so only lower limits could be placed on their column densities.

(Howk & Sembach 1999; Vladilo et al. 2001; Prochaska et al. 2002). Their conclusions were all roughly the same; that the ionization corrections for most elements were $\lesssim 0.2$ dex in most cases. Due to the smaller amount of H I in the sub-DLA systems, one might expect that they would show a greater amount of ionization.

Dessauges-Zavadsky et al. (2003) showed the ionization corrections for their sample of sub-DLA at $z > 1.8$ were, in general small, with < 0.2 dex corrections based on predictions of the Cloudy software package. The only absorber in their sample that showed significant signs of ionization effects was the $\log N_{\text{H I}} = 19.37$ sub-DLA in the spectrum of Q2155+1358 at $z_{\text{abs}} = 3.565$. The absorbers in the spectra of Q0826-2230 with $\log N_{\text{H I}} = 19.04$, Q1009-0026 with $\log N_{\text{H I}} = 19.48$, and Q1010-0047 with $\log N_{\text{H I}} = 19.81$ have the lowest column densities in our sample, and thus might be expected to require some ionization corrections.

To investigate further, we used the Cloudy software package to compute photo-ionization models assuming local thermodynamic equilibrium (LTE). Calculations were performed with version

C06.02.b of Cloudy, last described by Ferland et al. (1998). Grids of Cloudy models were computed assuming that the spectrum of ionizing radiation striking the cloud followed the form of the extra-galactic UV background of Haardt & Madau (Haardt & Madau 1996; Madau, Haardt, & Rees 1999) at the appropriate redshift of the absorber, plus the model stellar atmosphere of Kurucz with a temperature of 30,000K to simulate a radiation field produced via an O/B-type star. Plots of both types of spectra can be found in Hazy, the documentation for Cloudy. The extra-galactic spectrum of Haardt & Madau is a harder spectrum than the Kurucz spectrum, which produces few photons with $h\nu > 2$ Ryd. In fact, the Haardt & Madau spectrum produces a total of ~ 21.13 times as many photons with $h\nu > 13.6$ eV than the Kurucz spectrum. From 1-2 Ryd though, the total ionizing photons is almost identical for both spectra. It has recently been shown that the contribution from local sources to the ionization of DLA systems is likely non-negligible compared to the ionizing background radiation field (Schaye 2006). We include the radiation field of the Kurucz stellar spectrum in these Cloudy simulations, but do not allow that intensity to vary relative to QSOs. In addition, our Cloudy models have included both cosmic ray and cosmic microwave backgrounds. These simulations however do not include radiation from local shocks caused by supernovae, or compact sources such as white dwarfs or compact binary systems, all of which may contribute significantly to the ionizing radiation field. Explorations into contributions of various galactic sources is beyond the scope of this work.

For each of the grids of models, the ionization parameter defined by

$$U = \frac{n_{\gamma}}{n_{\text{H}}} = \frac{\Phi_{912}}{cn_{\text{H}}},$$

(where Φ_{912} is the flux of radiation with $h\nu > 13.6$ eV) was increased from $\log U = -6.0$ to 0. Each model was tailored to match the $N_{\text{H I}}$, metallicity based on Zn II, and redshift of the observed system. Due to the saturation of the strong Al II λ 1670 transition, for each of the three systems where we have detections of Al III $\lambda\lambda$ 1854, 1862 lines only an upper limit can be placed on the ionization parameter U . Also, we are not at all able to constrain the shape of the ionizing spectrum that is illuminating the cloud. The possibilities presented here are but a myriad of other possible shapes of the spectrum of ionizing radiation. Nonetheless, using standard assumptions, outlined above, some conclusions can be drawn.

Cloudy models were calculated for all of the systems observed. We present the results of the most interesting systems here. With $\log N_{\text{H I}} = 19.04$ the weak sub-DLA toward Q0826-2230 may be expected to require ionization corrections. The only element observed in this system with multiple ionization stages was Mg. Due to the saturation of the Mg II $\lambda\lambda$ 2796, 2803 lines only a lower limit could be placed on the Mg^+ to Mg^0 ratio, and thus a lower

limit on the ionization parameter U . However, the Mg II λ 2803 line was not optically thick even in its strongest components, so the column density given in table 12 may not be far from true. To see if the true column density could be significantly higher, we increased the column densities in the components by a factor of 10, at which point there was significant deviation between the observed and theoretical profiles. Also, the column densities derived from the AOD method and profile fitting agreed to within 0.05 dex. Nonetheless, as can be seen from figure 10, the ionization corrections to Zn^+ are $\lesssim 0.2$ dex even for $\log U \lesssim -3.0$ which is the typical upper limit for other sub-DLA systems observed. We have therefore not included any ionization correction factor into the quoted Zn abundance in table 13.

In figure 10, the horizontal lines in the center panels indicates the observed limits or ratios of the Mg II to Mg I, Al III to Al II, and Al III to Fe II column densities. The vertical lines are therefore the corresponding ionization parameters based on these values. Based on the Mg II to Mg I ratio in the $z_{\text{abs}} = 0.9110$ sub-DLA in the spectrum of Q0826-2230, the ionization parameter is a lower limit due to the saturation of the Mg II lines.

The $\log N_{\text{H I}} = 19.48$ system in Q1009-0026 may also require ionization corrections. The Al II λ 1670 line was below the wavelengths accessible with the MIKE spectrograph, but we the Al III $\lambda\lambda$ 1854, 1862 lines were observed. We were therefore able to constrain the ionization parameter based on the Al III to Fe II ratio, which was $\log(\text{Al III} / \text{Fe II}) = -1.66$, and consequently based upon the Cloudy models $\log U = -3.70$. The ionization correction for Zn^+ based on this ionization parameter is small (~ 0.15 dex), so no correction corrections were introduced into table 13.

The $\log N_{\text{H I}} = 19.81$ system in the spectrum of Q1010-0047 is another system with relatively low $N_{\text{H I}}$ that may require ionization corrections. For this system, both the Al II λ 1670 and the Al III $\lambda\lambda$ 1854, 1862 lines were observed. The Al II λ 1670 line is saturated, so only an upper limit could be placed on the Al^{++} to Al^+ ratio. From the Cloudy models, the ionization parameter $\log U \lesssim -4.15$. Again, the ionization corrections for Zn^+ were small for values within the range of possible values for U , so no ionization correction was added to the values in table 13.

In general, from results of the Cloudy modeling the ionization parameter U is typically small, $\log U \lesssim -3.0$ for the systems that had detections of the Al II λ 1670 and Al III $\lambda\lambda$ 1854, 1862 lines. We note, again, that the ionization parameter does depend strongly on the shape of the ionizing spectrum.

It has been mentioned before that the Al III to Al II ratio may not be an accurate predictor of the ionization state of the gas observed in QSO absorption line systems (Prochaska et al. 2002). One of the reasons for this is the uncertainties in the atomic data for Al. It has been suggested that the Al III to Al II ratio may provide an estimate of the ionization of the gas in DLAs to first order, but better diagnostic indicators of the ionization state of the gas are the Fe^{++} to Fe^+ and N^+ to N^0 ratios. For the absorbers presented here the lines of these ions are well in the UV therefore could not be observed with our ground based observations. Therefore the Al III to Al II ratio is the only opportunity available to study the ionization state of the gas in these sub-DLA systems. Even if we cannot derive the ionization parameter absolutely, it appears that the ionization of the components does not change over a wide range of integrated column densities and redshifts. It should be noted that for the systems in which Al II was not observed there is no indication that Al^{++} is the dominant ion. As can be seen in table 14, the Mg II to Al III ratio is similar for systems with and without Al II measurements. If Al III were relatively higher in one sys-

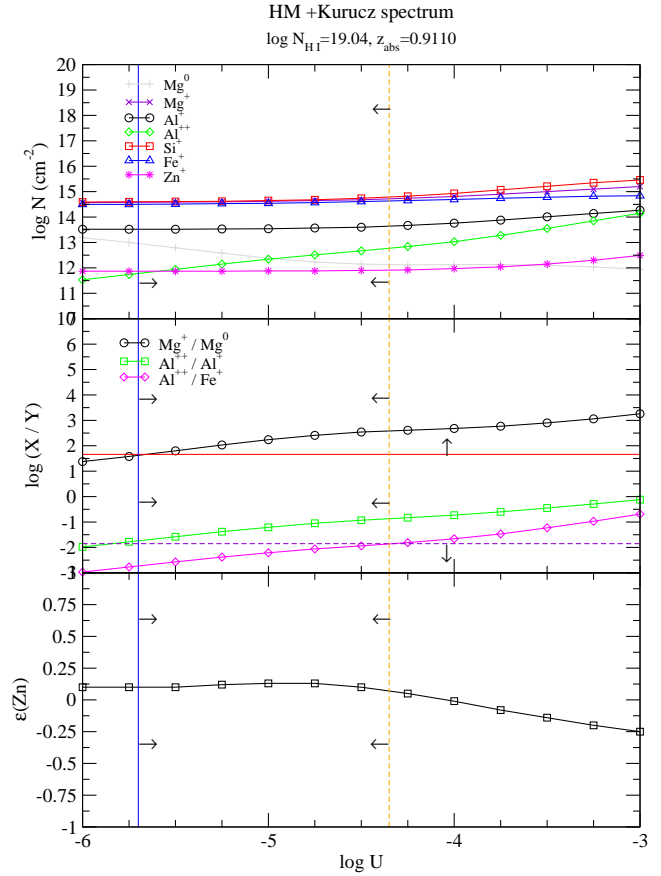


Figure 10. Results of the Cloudy simulations for the $z = 0.9110$ sub-DLA with $\log N_{\text{H I}} = 19.04$ in the spectrum of Q0826-2230. The upper panel shows the column densities for several species of interest. The middle panel shows the logarithmic ratio of Mg^+ to Mg^0 , $\text{Al}^{++}/\text{Al}^+$, and $\text{Al}^{++}/\text{Fe}^+$. Here, the horizontal solid red line indicates the lower limit to the observed ratio of the column densities derived from the Mg I λ 2852 line, and the Mg II $\lambda\lambda$ 2796, 2803 doublet. The vertical solid blue line is then the lower limit of the ionization parameter U , based upon the Cloudy modeling. The dashed lines show the observed Al III to Fe II ratio (purple), and the corresponding upper limit to the ionization parameter (yellow). The lower panel shows the ionization correction factor for Zn^+ in dex.

tem than the others, the limit of Mg II / Al III would be lower than the others. The use of the Al III / Fe II ratio in determining the ionization parameter may introduce some uncertainties. While Cloudy assumes solar abundances, differential depletion between Al and Fe may lead to an underestimation of the Al III / Fe ratio. In the Galaxy, Al is sometimes seen to be more depleted than Fe (Barker et al. 1984). Another source of uncertainty are nucleosynthetic mismatches between these two elements. The use of column densities from adjacent ions such as Al III and Al II, or Mg II / Mg I assumes that the ions coexist in the gas from which these lines arise. This is almost universally true in the case of Al III and Al II, the line profiles are very similar. The line profiles for Mg II and Mg I are not always as similar, especially in the components at higher radial velocities where Mg II lines are often seen without any components seen in the Mg I profile. The “core” components however typically do match very well, as can be seen in figures 1-8.

5.4 Sub-DLAs and the velocity dispersion-metallicity relationship

Based on a sample of $\sim 53,000$ star-forming galaxies at $z \sim 0.1$ observed in imaging and spectroscopy in the SDSS, Tremonti et al. (2004) discovered a mass-metallicity relationship for these galaxies. Specifically, they found a correlation between stellar mass and metallicity that spans over 3 orders of magnitude in stellar mass and one order of magnitude in metallicity. Nestor et al. (2003) noticed a relation between the width of Mg II and the metallicity, and suggested that the Mg II line width might be an indicator that the gas was in a deep potential well. Evidence has recently been provided for the possible existence of a mass metallicity relationship for DLA absorbers, assuming the velocity width of optically thin lines to be proportional to the mass (Ledoux et al. 2006). As a proxy for the stellar mass of these systems, which has been difficult to detect, the velocity width is used as an indicator of galaxy mass, as it potentially probes the depth of the gravitational potential well of the DLA systems. Bouché et al. (2006) however find an anti-correlation between the Mg II equivalent width, and the estimated halo mass based upon an indirect mass indicator.

Following the analysis of Ledoux et al. (2006), we performed an analysis of the apparent optical depth (see e.g., Savage & Sembach (1996)) of these sub-DLA systems. The apparent optical depth is defined as

$$\tau(\lambda)_a = \ln[I_0(\lambda)/I_{obs}(\lambda)],$$

where $I_0(\lambda)$ is the continuum level, and $I_{obs}(\lambda)$ is the observed intensity. Specifically, we defined the beginning of the absorption line systems profile as the point where the apparent optical depth of the line reached a value of 3σ higher than the average noise value in the continuum. Similarly, the upper edge was defined as the point where the apparent optical depth dropped below the 3σ level of the continuum. In figures 13 and 14, we give the apparent optical depth of the Fe II λ 2374 lines vs. the radial velocity widths defined here for the systems in this sample.

In figure 15 we plot the metallicity vs velocity for the DLA absorbers from Ledoux et al. (2006) (open circles); sub-DLAs from Ledoux et al. (2006) (open squares); sub-DLAs from Péroux et al. (2006a), Péroux et al. (2006b), & Prochaska et al. (2006) (filled squares); DLAs from Péroux et al. (2006a) & Péroux et al. (2006b) (filled circles); the Zn detections from this work (filled stars); and the upper limits from this work (downward arrows). In their analysis, Ledoux et al. (2006) used weaker features, where at most 40% of the continuum level was absorbed by the line. Due to the unavailability of the spectra for the sub-DLAs in the literature, we were unable to measure the velocity width directly, and the value plotted is the velocity width given in the reference. In the case of the two sub-DLAs in Prochaska et al. (2006), the velocity width was estimated from the plots of the Si II λ 1808 and Fe II λ 1608 lines. For the systems in our sample and Péroux et al. (2006a,b), in addition to the Fe II λ 2374 line we also measured the velocity width of the Mg II λ 2796 or λ 2803 line, which is also plotted for each system in figure 15, with a line connecting the two values. We have chosen these two lines for this investigation for the several reasons. Firstly, with weaker features, the velocity width becomes sensitive to the S/N. Secondly, the Fe II λ 2374 line looks much like Ca II in the SMC, so ground based work with Ca II in lower z systems can be compared directly with the Fe II λ 2374 line in higher z systems. Lastly, the stronger Mg II λ 2796, 2803 lines represent a maximum velocity width to the line, and also include the

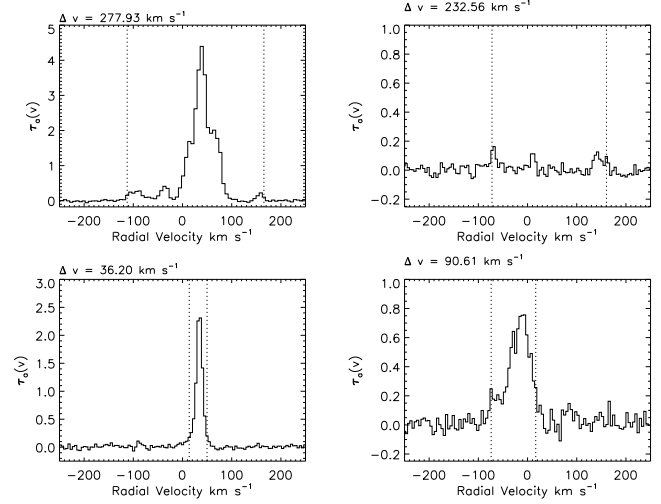


Figure 11. Apparent Optical Depth plots for the Fe II λ 2374 line for (clockwise from top left); the $z_{abs} = 1.4051$ system in Q0354-2724, the $z_{abs} = 0.9110$ system in Q0826-2230, the $z_{abs} = 0.8866$ system in Q1009-0026, and the $z_{abs} = 0.8426$ system in Q1009-0026. The total velocity width for the system, defined in § 5.3, is given above the plot.

components at higher radial velocities that are often not seen in the intrinsically weaker features.

As can be seen from figure 15, the systems from this sample are in agreement with the general trend of the data. More interesting though is the fact that the sub-DLAs from this sample and from Prochaska et al. (2006); Péroux et al. (2006a) are all at the highest end of the metallicity range. Indeed, the only points that lie above solar metallicity are those from sub-DLAs. Is this possible evidence that sub-DLAs are more representative of massive spiral or elliptical galaxies than their DLA counterparts? See also Khare et al. (2006) for a discussion of the nature of QSO absorbers.

Because the absorbers chosen in our sample were chosen partly because of their strong Mg II or Fe II lines, it is possible that these systems would be disposed to lie in the upper right corner of figure 14, with high metallicities and larger velocity widths. It was, however, shown that W_{MgII} does not correlate with $[Zn/H]$ (Kulkarni et al. 2007) based on individual measurements. The isolation of points in this region is therefore a real effect.

6 CONCLUSIONS AND FUTURE WORK

In this paper, we have presented high-resolution abundance measurements of 7 sub-DLAs and 1 DLA. Several of these systems show moderately high levels of metal enrichment compared to DLAs, with three having near solar or super-solar abundances. To date, the higher HI column density DLA systems with $\log N_{HI} > 20.3$ have been studied preferentially due to their high gas content and therefore possible high metal content. However, these systems show low metallicities at any redshift with $[Zn/H] \sim -1.0$ dex. Of all the (mainly neutral) QSO absorbers studied to date, all eight that have been observed with super-solar metallicities are all sub-DLAs (Pettini et al. 2000; Khare et al. 2004; Péroux et al. 2006a; Prochaska et al. 2006). From the results of the Cloudy modeling presented here, the ionization corrections for these absorbers in general appear to be low, consistent with the ionization corrections found by Dessauges-Zavadsky et al. (2003) for the sub-DLAs at higher redshift. We note however that the shape of the ioniz-

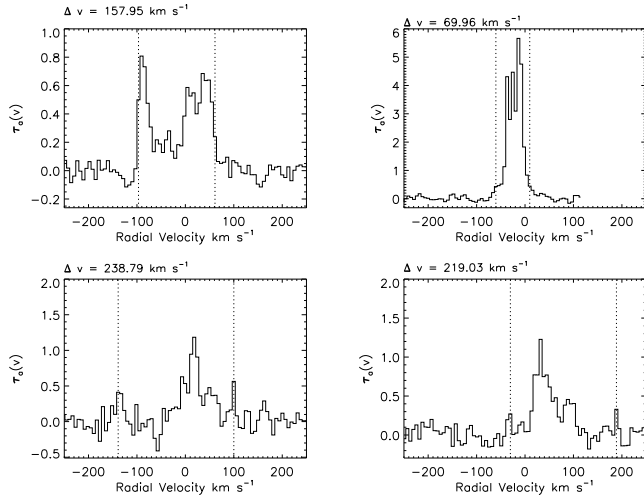


Figure 12. Same as figure 13, but for the $z_{\text{abs}} = 1.3270$ system in Q1010-0047, the $z_{\text{abs}}=1.2346$ system in Q1224+0037, the $z_{\text{abs}}=1.1414$ system in Q2331+0038, and the $z_{\text{abs}}=1.2665$ system in Q1224+0037

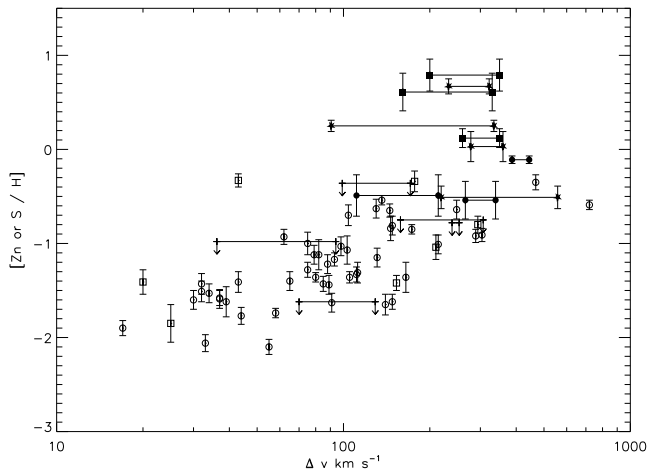


Figure 13. The metallicity vs velocity width for the DLA absorbers from Ledoux et al. (2006) (open circles); sub-DLAs from Ledoux et al. (2006) (open squares); sub-DLAs from Péroux et al. (2006a), Péroux et al. (2006b), & Prochaska et al. (2006) (filled squares); DLAs from Péroux et al. (2006a) & Péroux et al. (2006b) (filled circles); the Zn detections from this work (filled stars); and the upper limits from this work (downward arrows). For the absorbers in this sample and for the absorbers in Péroux et al. (2006a) & Péroux et al. (2006b), we measured the velocity width from both the Fe II λ 2374 line as seen in figures 13 and 14, and also the stronger Mg II $\lambda\lambda$ 2796,2803 lines. These two values are plotted in figure 15 with a line connecting the two points.

ing spectrum did strongly effect the ionization corrections from the Cloudy models, so the true ionization corrections could possibly be much larger. We have based our calculations on the radiation fields currently thought to be most relevant. Conditions will vary from component to component, and from system to system based on their respective temperatures and densities, and on the proximity or not of X-ray sources, UV stellar sources, and UV emission from shocks. The input spectrum is therefore certainly a source of uncertainty, but other input parameters ranging from atomic data to the morphology assumed by Cloudy in modeling DLA systems are likely sources of uncertainties.

On the matter of the high (i.e. super-solar) abundances, the er-

rors for all our values are based on formal errors. We cannot quantitatively evaluate possible sources of error from external sources outside the range of the assumptions used in the analysis of $N_{\text{H I}}$ and the ionization corrections. The matter of $N_{\text{H I}}$ determinations is discussed in the appendix, and ionization corrections are discussed in § 5.3. The former requires higher resolution, higher S/N UV spectra to improve the confidence in the errors, and the latter requires a much more detailed knowledge of the radiation field in the absorbers as well as the geometry. $N_{\text{H I}}$ determinations could potentially be improved when HST is refurbished with UV spectroscopic capability. The ionization corrections are more difficult to determine, and will need to be continually improved when more is learned about the environment of the absorbers. For the moment, we urge caution when interpreting the highest abundances, until more cases are verified or these two matters are more fully dealt with.

The errors reported in table 12 are based upon the errors given by Rao, Turnshek, & Nestor (2006), with no ionization corrections. Taking the errors for $N_{\text{H I}}$, conservatively estimated in the appendix, our estimates on the ionization correction from the cloudy modelling, and the error on $N_{\text{Zn II}}$, the metallicities for the $z_{\text{abs}}=0.9110$ and $z_{\text{abs}}=0.8866$ sub-DLAs in Q0826-2230 and Q1009-0026 are $+0.68 \pm 0.17$ and $+0.25 \pm 0.16$ respectively with the errors added in quadrature. We have however presented arguments that the observed trends in ion ratios over large ranges of $N_{\text{H I}}$ make our conclusions valid, for the purposes of this paper.

Although progress has been made recently in the understanding of sub-DLA absorbers, more observations are needed to fully understand the role of sub-DLAs in the metal enrichment history of the universe. Aside from the two absorbers in Péroux et al. (2006a,b), our measurements constitute the only available high resolution data available for sub-DLAs at $z < 1.5$. As was pointed out in Prochaska et al. (2006), these very metal rich sub-DLAs may be rare, but even if they are $\lesssim 1\%$ of the total population they will contribute significantly to the mean metallicity because of the much larger number density of sub-DLA systems. Clearly, more observations are needed to determine how common metal-rich sub-DLAs are, to see if sub-DLAs do harbor a large fraction of the missing metals, and to extend the mass-metallicity relationship for QSO absorbers to include more sub-DLAs. Future HST observations would allow us to better determine the ionization corrections using the Fe III λ 1122, N II λ 1084, and N I $\lambda\lambda$ 1134, 1199 lines respectively. The two transitions of S III ($\lambda\lambda$ 1012, 1190) provide a more likely unblended source of lines that can be used to check for ionization corrections, though S III probes somewhat harder radiation fields than Fe III and N II.

ACKNOWLEDGMENTS

Thanks to the anonymous referee for the helpful comments that improved this work. We thank the helpful staff of Las Campanas Observatory for their assistance during the observing runs. Thanks to J.X. Prochaska for his help with the MIKE reduction software. We thank Gary Ferland for both developing the Cloudy code and for answering questions concerning Cloudy simulations. Thanks to S.M. Rao and D. Turnshek for discussions about fitting the Ly- α profiles. We thank Don Lamb and Jim Truran for enlightening discussions on SNe enrichment. J. Meiring and V.P. Kulkarni gratefully acknowledge support from the National Science Foundation grants AST-0206197 and AST-0607739, and the NASA/STScI grant GO-

9441. J. Meiring acknowledges partial support from South Carolina Space Grant graduate student fellowship.

APPENDIX - N_{HI} DETERMINATIONS

The systems studied in this work all have known N_{HI} from HST spectra. Here we provide plots of the Voigt profiles of the Lyman- α transition using the best fit values of the column density from Rao, Turnshek, & Nestor (2006). Due to the low resolution and S/N of these UV spectra, only one component was used in the fits. Several factors such as blending with Lyman- α forest lines, continuum fitting and component placement add difficulties to the profile fitting with these spectra. These effects are largely unknown in each case and formal errors that account for a wide range of possibilities cannot be made until there are higher S/N UV spectra from the refurbished Hubble Space Telescope. We show in figures 14 and 15 the Voigt profiles corresponding to the column densities given by Rao, Turnshek, & Nestor (2006) and convolved with the instrumental spread function, superimposed on the archival data from HST cycle 6 program 6577, cycle 9 program 8569, and cycle 11 program 9382. We note that the normalization, i.e., the continuum fit that we define may differ from that adopted by Rao, Turnshek, & Nestor (2006). For our continuum fits, a polynomial typically of order $\lesssim 6$ was used, and the absorption line itself was excluded from the fitting region. Also over-plotted are profiles with H I column densities smaller and larger by 0.15 dex. For the sub-DLAs in our sample, the plots are not in print, and we include the DLA for completeness. In some cases, the errors cited by Rao, Turnshek, & Nestor (2006) may not cover the revised values from higher resolution, higher S/N data, and the plotted range gives an idea of how much things may change. However, we find the fits and errors in column density from Rao, Turnshek, & Nestor (2006) to be completely satisfactory, and have used them in the body of the text. In cases where the profiles with error profiles that seem to fit slightly better, there is no systematic sense of the differences: in some cases the H I column density is smaller, and in others it is larger. This may imply that our values of $[\text{Zn}/\text{H}]$ may need revision later, when higher quality data become available. In particular, the system in Q0826-2230 may have a slightly higher value of N_{HI} and therefore slightly lower $[\text{Zn}/\text{H}]$. However, the value would still be $\sim 2\times$ solar. The conclusions of this paper would not be changed by any likely changes in the values of N_{HI} .

REFERENCES

Barker E.S., Lugger P.M., Weiler E.J., York D.G., 1984, *ApJ*, 280, 600
 Bernstein R., Schechtman S.A., Gunnels S., Mochnacki S., Athey A., 2003 *SPIE*, 4841, 1694
 Bouche N., Murphy M.T., Pèroux C., Csabai I., Wild V., 2006, *MNRAS*, in press
 Chen H-W., Lanzetta K.M., 2003, *ApJ*, 597, 706
 Dessauges-Zavadsky M., Peroux C., Kim T.S., D’Odorico S., McMahon R.G., 2003, *MNRAS*, 345, 447
 Ellison, S., 2006, *MNRAS*, 368, 355
 Falomo R., 1990 *ApJ*, 353, 114
 Ferland G. J., Korista K.T., Verner D.A., Ferguson J.W., Kingdon J.B., Verner E.M., 1998, *PASP*, 110, 761
 Gharanfoli S., Kulkarni V.P., 2006, *ApJ*, submitted

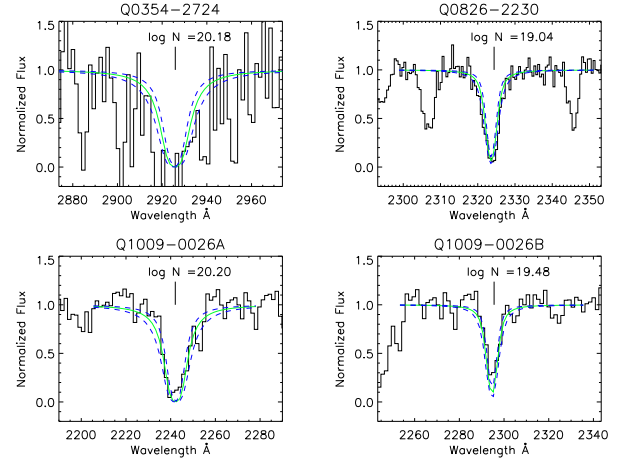


Figure 14. UV spectra for the systems, clockwise from the top left; $z_{abs}=1.4051$ system in Q0354-2724, $z_{abs}=0.9110$ in Q0826-2230, $z_{abs}=0.8866$ in Q1009-0026, and $z_{abs}=0.8426$ in Q1009-0026. The central green solid profile in each plot is for the best fit value from Rao, Turnshek, & Nestor (2006), and in the blue dashed profiles above and below, the column density was modified by 0.15 dex. The vertical tick mark above the profile represents the absorption center of the metal lines. Note the different abscissa in the individual figures.

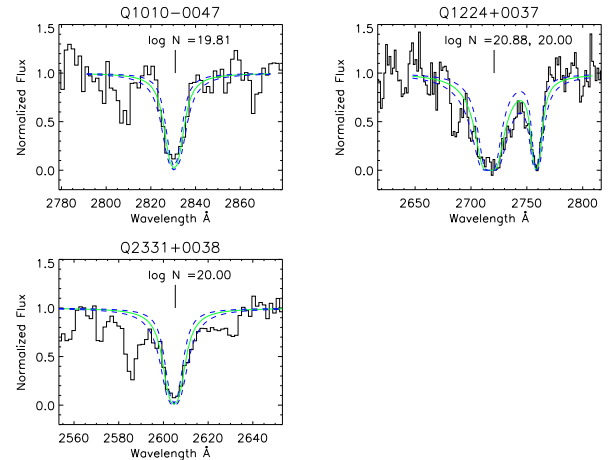


Figure 15. Same as figure 14, but for clockwise from the top left; $z_{abs}=1.3270$ in Q1010-0047, $z_{abs}=1.2346$ and $z_{abs}=1.2665$ in Q1224+0037, and $z_{abs}=1.1414$ in Q2331+0038.

Gratton R.G., Caretta E., Claudi R., Lucatello S., Barbieri M., 2004, *A&A*, 404, 187
 Haardt F., Madau P., 1996, *ApJ*, 461, 20
 Herbert-Fort S., Prochaska J.X., Dessauges-Zavadsky M., Ellison S.L., Howk J.C., Wolfe A.M., Prochter G.E., 2006, *PASP*, 118, 1077
 Hopkins A.M., Rao S.M., Turnshek D.A., 2005, *ApJ*, 630, 108
 Howk J.C., Sembach K.R., 1999, *ApJ*, 523, L141
 Khare P., Kulkarni V.P., Lauroesch J.T., York D.G., Crotts P.S., Nakamura O., 2004, *ApJ*, 616, 86
 Khare P., Kulkarni V.P., Pèroux C., York D.G., Lauroesch J.T., Meiring J.D., 2006, *A&A*, submitted
 Kulkarni V.P., Fall S.M., Lauroesch J.T., York D.G., Welty D.E., Khare P., Truran J.W., 2005, *ApJ*, 618, 68
 Kulkarni V.P., Khare P., Pèroux C., York D.G., Lauroesch J.T.,

Meiring J.D., 2007, ApJ, in press
 Lodders, K., 2003, ApJ, 591, 1220
 Ledoux C., Petitjean P., Srianand R., 2003, MNRAS, 346, 209
 Ledoux, C. Petitjean, P., Moller, P., Fynbo, J., Srianand R., 2006, A&A, 457, 71
 Madau P., Haardt F., Rees M.J., 1999, ApJ, 514, 648
 Meiring J.D., Kulkarni V.P., Khare P., Bechtold J., York D.G., Cui J., Lauroesch J.T., Crotts A.P.S., Nakamura O., 2006, MNRAS, 370, 43
 Morton D.C., 2003, ApJS, 149, 205
 Nestor D.B., Rao S.M., Turnshek D.A., Vanden Berk D., 2003, ApJ, 595, L5
 Nestor D. B. 2004, Ph.D. thesis, Univ. Pittsburgh
 O'Meara J.M., Prochaska J.X., Burles S., Prochter G., Bernstein R.A., Burgess K., 2006, ApJ, in press
 Péroux C., Storrie-Lombardi L., McMahon R., Irwin M., & Hook I., 2001, AJ, 121, 1799
 Péroux C., Dessauges-Zavadsky M., D'Orico S., Kim T.S., McMahon R., 2003, MNRAS, 345, 480
 Péroux C., McMahon R.G., Storrie-Lombardi L.J., Irwin M.J., 2003, MNRAS, 346, 1103
 Péroux C., V.P. Kulkarni, J. Meiring, R. Ferlet, P. Khare, J.T. Lauroesch, G. Vladilo, D.G. York, 2006, A&A, 450 53
 Péroux C., Meiring J., Kulkarni V.P., Ferlet R., Khare P., Lauroesch J.T., Vladilo G., York D.G., 2006, MNRAS, 372, 369
 Petitjean P., Webb J.K., Rauch M., Carswell R.F., Lanzetta K., 1993, MNRAS, 262, 499
 Petitjean P., Rauch M., Carswell R.F., 1994, A&A, 291, 29
 Pettini M., Ellison S.L., Steidel C.C., Shapley A.E., Bowen, D.V., 2000, ApJ, 532, 65
 Prochaska J.X., Wolfe A.M., 2002, ApJ, 566, 68
 Prochaska J.X., Howk J.C., O'Meara J.M., Tytler D., Wolfe A.M., Kirkman D., Lubin D., Suzuki N., 2002, ApJ, 571, 693
 Prochaska J.X., O'Meara J.M., Herbert-Fort S., Burles S., Prochter G.E., Bernstein R.A., 2006, ApJL, in press (astro-ph/0606573)
 Rao S.M., Turnshek D.A., Nestor D.B., 2006, ApJ, 636, 610
 Rigby J.R., Charlton J.C., Churchill C.W., 2002, ApJ, 565, 743
 Sargent W. L. W., Steidel C. C., Boksenberg A., 1989, ApJS, 69, 703
 Savage B.D., Sembach K.R., 1991, ApJ, 151, 313
 Savage B.D., Sembach K.R., 1996, ApJ, 379, 245
 Savaglio, S. et al. 2005, ApJ, 635, 260
 Schaye J., 2006, ApJ, 643, 59
 Schneider D.P., Hall P.B., Richards G.T., Vanden Berk D.E., Anderson S.F., Fan X., Jester S. Stoughton C., Strauss M., et al., 2005, AJ, 130, 367
 Sembach K.R., Savage B.D., 1996, ApJ, 457, 211
 Tremonti C. A. et al. 2004, ApJ, 613, 898
 Vladilo G., Centurión M., Bonifacio P., Howk C., 2001, ApJ, 557, 1007
 Welty D.E., Hobbs L.M., York D.G., 1991, ApJS, 75, 425
 Welty D.E., Hobbs L.M., Lauroesch J.T., Morton D.C., Spitzer L., York D.G., 1999, ApJS, 124, 465
 Wolfe A.M., 1993, ApJ, 402, 411
 York D.G., Dopita M., Green R., Bechtold J., 1986, ApJ, 593, 215
 York D.G., Vanden Berk D., Richards G.T., Crotts A.P.S., Khare P., Lauroesch J.T., Lemoine M., et al., 2005, IAU Colloquium proceedings 199, Probing Galaxies through Quasar Absorption Lines, Williams P.R., Shu C., Menard B., Cambridge University Press, Cambridge
 York D.G., Khare P., Vanden Berk D., Kulkarni V.P., Crotts A.P.S.,

Lauroesch J.T., Richards G.T., et al., 2006, MNRAS, 367, 945

This paper has been typeset from a \LaTeX file prepared by the author.